Crystal field effects on the photoemission spectra in Cr2O3 thin films: from multiplet splitting features to the local structure

Pamella Vasconcelos, Alain Chartier, Jean-Baptiste Moussy, Denis Menut, Frédéric Miserque

Crystal field effects on the photoemission spectra in Cr$_2$O$_3$ thin films: from multiplet splitting features to the local structure

Pâmella Vasconcelos Borges Pinho[a,*], Alain Chartier[a,*], Jean-Baptiste Moussy[b], Denis Menut[c], Frédéric Miserque[a]

a DEN – Service de la Corrosion et du Comportement des Matériaux dans leur Environnement (SCCME), CEA, Université Paris-Saclay, F-91191 Gif-sur-Yvette, France

b Université Paris-Saclay, CEA, CNRS, SPEC, 91191, Gif-sur-Yvette, France

c Synchrotron SOLEIL, L'Orme des Merisiers, Saint Aubin BP 48, 91192 Gif-sur-Yvette, France

*E-mail: pamella.vasconcelos@cea.fr; alain.chartier@cea.fr

ABSTRACT: Changes in the shape of X-ray photoemission (XPS) spectra can be related to changes in the local structure of a transition metal. By combining Crystal Field Multiplet calculations and well-controlled molecular beam epitaxy growth of α-$Cr_2O_3(0001)$ thin films on α-$Al_2O_3(0001)$ substrates, we prove that it is possible to link the features of Cr $2p$ XPS spectra with local distortions of CrO_6 octahedra and d-orbitals reorganization. Hence, we show that the splitting of the Cr $2p_{3/2}$ envelope is related to the degeneracy of the t_{2g} orbital triplet, which corresponds to a fully relaxed structure. Conversely, the broad unstructured Cr $2p_{3/2}$ envelope relies on splitting of t_{2g} orbitals and it is the fingerprint of large trigonal distortions of CrO_6 octahedra. Then, using the Cr $2p$ XPS as a structural tool for α-Cr_2O_3, we show that the Cr_2O_3 protective layer formed by oxidation of polycrystalline Ni30Cr alloy exhibits in-plane strains at early oxidation stages and grows preferentially along the c-axis.

1. INTRODUCTION

Ni-Cr binary alloys are usually used for high temperatures applications due to their excellent mechanical properties and resistance to corrosion [1–3]. When exposed to oxidizing atmospheres, these alloys can develop a Cr_2O_3 protective layer that slows down the oxidation kinetic and extends the material lifetime. A number of studies have been performed to evaluate the growth kinetics and the microstructure of the oxide scales during oxidation of Ni-Cr binary alloys [4–6] and, recently, the focus has been on the early stages of the alloy oxidation [7,8]. It has been shown that the initial reactions control the continuous growth of the oxide coating and therefore actively influence the performance of the metallic alloy.

Owing to the thinness of the oxide layers formed on early stages of the alloy oxidation, the study of their chemical and microstructure evolutions can be very challenging. In this regard, surface sensitive analytical techniques, such as X-ray photoemission spectroscopy (XPS), have proven to be well suited for giving chemical insights into the growth of oxide layers [9,10]. Combined with structural information provided by diffraction techniques [11], one may obtain a rough understanding of the oxidation process [12,13].

Interestingly, the transition from the initial state of oxide nucleation to the thickening of complete Cr_2O_3 layers introduces changes in the binding energy and the multiplet splitting features of the Cr $2p$ XPS spectra. These changes rely on the evolution of the local structure of chromium. Yet, a comprehensive investigation of the XPS spectra acquired through the growth of chromium oxide is still lacking.

Accounting for the shape evolution of the Cr $2p$ XPS spectra of Cr_2O_3 compound is in fact a challenging task. Many-body effects, such as multiplet splitting and shake-up,

2

promote additional fine structure to the spectral core lines, drawing complex multi-peaks envelopes. For a long time, these extra peaks have complicated the understanding of the spectra, leading to diverse interpretations in literature [14]. Theoretical calculations of the multiplet structure have shown that this fine structure could be a useful tool to detect differences in surface chemistry [15]. The multiplet peaks are sensitive to changes in the local crystal field geometry, the formal oxidation state of the metal ion, or even to effects of charge transfer from back bonding [16].

The present work investigates the subtleties of the Cr $2p$ XPS spectrum acquired during the growth of the Cr_2O_3 protective layer on Ni30Cr alloy. A multi-electronic semi-empirical method is applied to understand the effect of the local crystal field geometry in the redistribution of intensity of the spectral lines. First, spectra from monocrystalline α-Cr_2O_3(0001) thin films are acquired to evaluate the crystal field parameters used in the theoretical calculations. Then, the problem is transposed to polycrystalline samples of Cr_2O_3 grown by exposing the Ni30Cr alloy to an oxygen-rich environment at high temperature. Here, the aim is to draw a comprehensive link between the chromium local geometry and its XPS spectral shape.

2. EXPERIMENTAL AND THEORETICAL DETAILS

2.1 Symmetry considerations

Chromium oxide, α-Cr_2O_3, crystallizes in a corundum-type structure described by the $R\bar{3}c$ space group [17]. The hexagonal unit cell (a = 0.492 nm and c = 1.37 nm) contains four formula units. The local Cr^{3+} site symmetry is a trigonal distorted octahedron with three Cr–O bonds of 1.97 Å length and three of 2.02 Å, and two O–Cr–O angles of 81°24' and 99°00', as depicted on **Figure 1a**. The Cr^{3+} is displaced (upward in **Figure 1a**) along the C_3 axis relative to the octahedral center, making two equilateral triangles formed by three oxygen ions each. Due to a slight rotation of the upper and lower oxygen ions triangles (**Figure 1b**), the exact symmetry of the Cr^{3+} environment in α-Cr_2O_3 is C_3. However, since the angle of rotation is very small (about 2°57'), the system can be reasonably approximated by the C_{3v} point group [18–20].
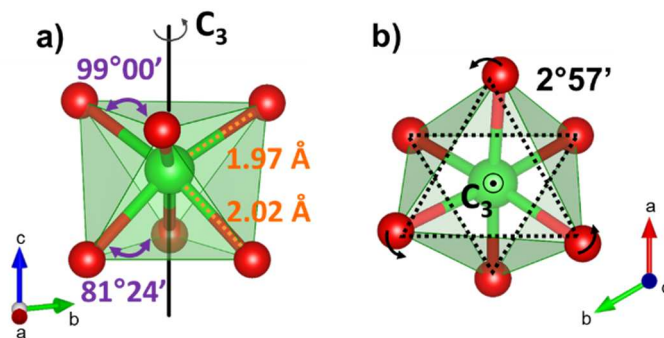
Figure 1. Representations of the Cr^{3+} local site in α-Cr_2O_3 along two different crystallographic orientations. The bond distances (orange) and O–Cr–O angles (purple) are represented in (a). The rotation angle between the upper and lower triangle (black dotted line) are represented in (b). Color coding: Cr (green) and O (red).

4

2.2 Preparation of Cr₂O₃ samples

Epitaxial thin films of α-Cr_2O_3(0001) of different thicknesses were grown on α-Al_2O_3(0001) monocrystalline substrates by Oxygen-plasma-assisted Molecular Beam Epitaxy (O-MBE) [21], as detailed in the Supporting Information. Reflection high-energy electron diffraction (RHEED) patterns were monitored in real time during the growth of each sample (**Figure S1**) in order to control the crystalline structure of the atomic layers. The number of monolayers (ML) was calibrated *in situ* using a quartz balance (Cr evaporation rate around 0.26 $Å \cdot min^{-1}$) and confirmed *ex situ* by X-ray reflectivity measurements (**Figure S2**). Here, one ML has a thickness of 0.23 nm, which includes one close-packed layer of O and 2/3 ML of Cr in the corundum (0001) direction. Two samples were grown: one made of 5 ML (*i.e.* 1.1 nm) and the other of 23 ML (*i.e.* 5.3 nm). Following the growth, the phase and crystalline quality of the films were verified by X-ray diffraction (**Figure S3**). Then, *ex situ* XPS measurements were performed (see Results and Discussion).

Polycrystalline samples were prepared by exposing a polished Ni30Cr sheet (5 x 10 mm^2, 99.5% in purity) to a controlled leak of oxygen. In order to remove any surface contaminations and the native oxide layer, the alloy sample was cleaned *in situ* by Ar^+ sputtering. Then, the oxidation was performed at 700 °C under 1 x 10^{-5} mbar of pure O_2 atmosphere. The growing of the oxide layer was followed by *in situ* X-ray photoemission spectroscopy (XPS) measurements, acquired with parabolic time steps (*t* = 0, 1, 4, 9, 16, 25, 36 and 64 min) until no further changes were noticed in the spectral shape. As expected, only pure Cr_2O_3 layers were formed, without any oxidation of nickel (see Supporting Information). Thicknesses for 1 and 4 minutes were estimated by the attenuation of the Ni 2$p_{3/2}$ substrate peak (**Figure S4**) and subsequently extrapolated

using the Wagner-parabolic law (see Supporting Information). Herein, we estimated that the Cr_2O_3 layers obtained at 1, 4, 9, 16, 25 minutes have thicknesses of respectively 0.7, 4.4, 8.1, 11.8 and 15.5 nm.

2.3 X-ray Photoelectron Spectroscopy measurements

The X-ray Photoelectron Spectroscopy (XPS) analyses were carried out with an Escalab 250 XI (*Thermo Fisher Scientific Inc.*) using a monochromatic Al $K_α$ source (hν = 1486.6 eV). For the α-Cr_2O_3(0001) epitaxial thin films, a low-energy electron flood gun was used during spectral acquisition and the binding energies were corrected by fixing the contamination *1s* line of carbon at 285.0 eV. For the *in situ* Ni30Cr alloy oxidation, there was no need for charge compensation. High-resolution spectra were acquired using a 5 eV pass energy and an analysis spot of 900 µm of diameter. The data was treated using the commercial *Avantage* software (*Thermo Fisher Scientific Inc.*). A Shirley-type background was used for all spectra.

2.4 Crystal Field Multiplet calculations

Semiempirical crystal field multiplet (CFM) calculations were performed to simulate chromium *2p* XPS spectra using the quantum many-body script code Quanty [22–24] within the graphical interface Crispy [25]. In CFM theory [26–28], the solid system is mimicked by considering the transition metal as an isolated ion embedded in a crystal-field potential. The multi-electronic states are described in terms of the *3d–3d* and *2p–3d* Coulomb (F^k_{dd}, F^k_{pd}) and exchange (G^k_{pd}) interactions, the *2p* ($ζ_{2p}$) and *3d* ($ζ_{3d}$) spin-orbit coupling, and the local symmetry. The Cr^{3+} electronic configurations of relevance in our description are *3d³* for initial states and *2p⁵3d³* for final states. In the Cr 2p XPS

6

of Cr_2O_3, the satellite peak assigned to charge transfer excitations sits close to the $2p_{1/2}$ position, broadening this line [29,30]. Since this zone of the spectrum is not interesting for our study (see Results and Discussion), additional electron configurations resulting from ligand charge transfer (*e.g. $3d^{n+1}\underline{L}$*) were neglected.

In order to account the iono-covalent behavior of the Cr-O chemical bond, the *ab initio* Hartree-Fock (HF) values of the Slater-Condon integrals were scaled down (see **Table 1**). The reduction factors of F^2_{dd} and F^4_{dd} for the initial state were obtained by comparison of the HF values with the ones determined by the experimental Racah B and C parameters ($B = 9F^2_{dd} - 5F^4_{dd}$ and $C = 5 F^4_{dd}/63$). For experimental B = 0.057 eV and C = 0.433 eV [31], the HF values of F^2_{dd} and F^4_{dd} are reduced by 54 % and 81 %, respectively. The same scaling factors were applied for F^2_{dd} and F^4_{dd} in the final state. For F^2_{pd}, G^1_{pd}, G^3_{pd} and ζ, the HF values were set according to literature. More details are available in literature [19,28] and in the Supporting Information.

The effects of the local symmetry are accounted by the crystal field (CF) parameters in the C_{3v} point group (Dq, $D\sigma$ and $D\tau$, following [32]). These parameters were fitted to the spectrum obtained in each oxidation stage. The procedure to optimize them and the link to the local electronic structure are discussed in the following section. As shown in **Table 1**, both Dq and $D\sigma$ have constant values, while $D\tau$ ranges from -0.33 up to -0.25 according to the thickness of the Cr_2O_3 sample.

For all simulated spectra, the ground state was populated according to a Boltzmann distribution at 300 K. The isotropic spectra were calculated by solving Green's functions in second quantization. The resulting sharp peaks were convoluted with a Lorentzian function (FWHM = 0.3 eV) and a Gaussian function (FWHM = 0.7 eV) to mimic the experimental broadening of the spectral lines.

Table 1. Energy values (in eV) and reduction factor of the electronic structure parameters of Cr^{3+} used for calculating the XPS spectra of Cr_2O_3. The value of $D\tau$ parameter varies according to the thickness of the Cr_2O_3 sample.

| Parameter	Ground state $3d^3$	Final state $2p^53d^3$	Reduction factor
F^2_{dd}	5.819	6.262	0.54
F^4_{dd}	5.471	5.890	0.81
F^2_{pd}	-	5.285	0.80
G^1_{pd}	-	3.876	0.80
G^3_{pd}	-	2.450	0.90
ζ_{2p}	-	5.668	1.00
ζ_{3d}	0.035	0.047	1.00
$10\,Dq$	2.08	2.08	-
$D\sigma$	0.60	0.60	-
$D\tau$	-0.33 to -0.25	-0.33 to -0.25	-

3. RESULTS AND DISCUSSION

3.1 *In situ* XPS of Ni30Cr oxidation

We start by depicting the oxidation of Ni30Cr as measured by XPS, from clean alloy up to 64 minutes under oxygen leak. Overall, **Figure 2** describes a typical evolution of the Cr 2p XPS spectrum with oxidation time, as already reported elsewhere [13]. Before exposure to oxygen (spectrum at the bottom), the XPS spectrum exhibits features of metallic chromium. We recognize two single asymmetrical peaks for Cr 2$p_{3/2}$ and Cr 2$p_{1/2}$ envelopes, centered respectively at 573.8 eV and 583.1 eV. Then, at the first stage of the oxidation (spectrum at 1 minute), two broad peaks – at 576.5 eV for Cr 2$p_{3/2}$ and at 586.1 eV for Cr 2$p_{1/2}$ – belonging to chromium oxide smoothly grow at the expense of the ones of metallic chromium. These peaks eventually take over after 4 minutes of oxygen exposure. The Cr 2p envelopes show complex multiplet structures (*e.g.* spectrum at 25 minutes), related to the coupling between the *2p* core-hole and the unpaired electrons in the *3d* outer shell.

For more than 4 minutes of oxidation and up to 64 minutes (not shown), minor changes in the multiplet splitting features are observed in the Cr *2p$_{1/2}$* envelope. Conversely, a striking splitting of the Cr *2p$_{3/2}$* envelope is discernable, along with a shoulder in the high-energy part (~ 577 eV) unveiled as the oxide layers grow. These features can be rationalized using a standard peak-fitting procedure [16]. Hence, the Cr 2p$_{3/2}$ envelope was fitted with five multiplet splitting peaks having FMHW of ~0.9 eV and separations of 0.6 to 1.0 eV. The peaks obtained are reported on **Figure 2** and their parameters are available in the Supporting Information (**Table S1**). We see that the binding energies of the multiplet peaks in the Cr *2p$_{3/2}$* envelope witness moderate evolutions: they decrease by only a few tenths of an eV. At the opposite, the intensities

of the peaks are considerably redistributed. This is particularly pronounced for the first and fourth peaks highlighted respectively in red and yellow in **Figure 2**. The intensity of first multiplet peak (~575 eV) increases from 20 % to 30 %, while the intensity of the fourth multiplet peak (~577 eV) decreases from 24 % to 15 %.
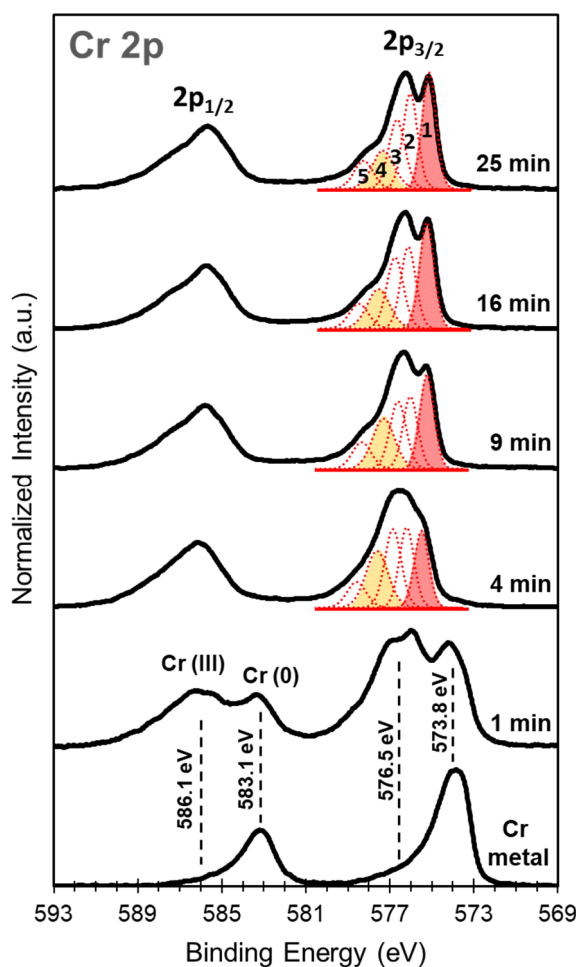
Figure 2. High-resolution Cr 2*p* XPS spectra as function of oxidation time of Ni30Cr alloy. For the spectrum of the Cr(III) oxide only ($t \geq 4$ min), the peak fitting of the Cr $2p_{3/2}$ envelope is depicted in dotted red lines. Highlighted the peak 1 (red) and the peak 4 (yellow), which present the major redistribution of intensity upon oxidation. The fitted spectra (not shown) follow the experimental line. In the fitting procedure, each multiplet splitting peak was convoluted with 30

% ratio of Lorentzian-Gaussian functions, preceded by a subtraction of the Shirley-type background.

3.2 *Ex situ* XPS of α-Cr₂O₃ epitaxial films

We now turn to the analysis of the Cr *2p* core-levels spectra for α-Cr$_2$O$_3$(0001) thin films with 5 ML (*i.e.* 1.1 nm) and 23 ML (*i.e.* 5.3 nm) of thickness reported on **Figure 3**. Interestingly, the general shape of both Cr 2p XPS spectra is comparable to the previous ones for Ni30Cr. The Cr *2p$_{1/2}$* envelope exhibits marginal changes as the film grows, while the Cr *2p$_{3/2}$* envelope shows significant evolution. We see a minor splitting of the Cr *2p$_{3/2}$* envelope for the 5 ML sample, comparable to the 9 minutes spectrum of Ni30Cr oxidation (**Figure 2**). This splitting becomes sizable for the 23 ML sample and a shoulder in the high-energy part of the peak accompanies it, this time looking similar to the 25 minutes spectrum of Ni30Cr oxidation.

For comparison sake, the 5 and 23 ML samples were also fitted using a similar set of Gaussian-Lorentzian curves used in the polycrystalline samples, and their parameters are available in the Supporting Information (**Table S2**). The monocrystalline samples show the same trend of spectral shape evolution during film growth than the polycrystalline samples. The binding energies of the multiplet peaks are nearly unchanged, whereas the intensities of the peaks are redistributed. The intensity of the first multiplet peak (~575 eV) increases from 26 to 31 % and the intensity of the fourth multiplet peak (~577 eV) decreases from 19 to 17 %, as the film grows.
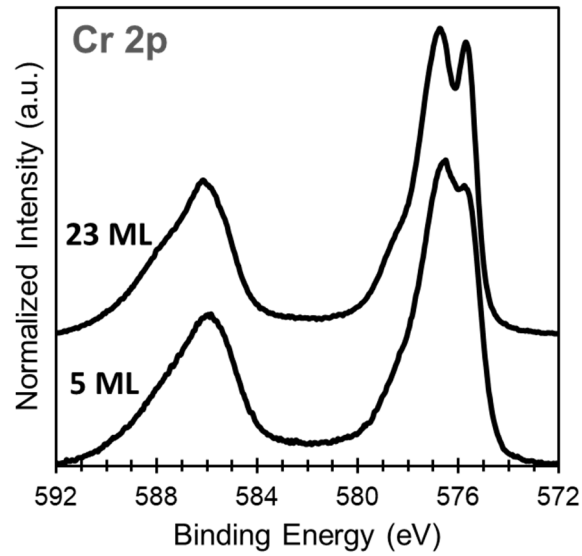
Figure 3. High-resolution Cr 2p XPS spectra for α-Cr₂O₃(0001) as a function of film thickness: at the top, 23 monolayers (23 M☐) and at the bottom, 5 monolayers (5 M☐).

Recalling that oxygen plasma leads to complete oxidation of chromium, XPS peaks can be attributed to only one oxidation state (Cr^{3+}). Additionally, the growth of epitaxial films follows only one crystallographic direction: structural changes can thus be easily evaluated. Therefore, both spectra provided by the 5 and 23 M☐ of α-Cr₂O₃(0001) films will be considered as references to adjust the crystal field parameters of the CFM model in the following section.

## 3.3 Crystal field parameters for epitaxial layers

The CF parameters (Dq, $D\sigma$ and $D\tau$) are obtained through a comparison between the experimental spectra of the epitaxial films (**Figure 3**) and the spectra calculated by means of the CFM model (**Figure 4**). In order to reduce the number of possible free adjustable parameters, Dq was set to the experimental value of 0.208 eV [31]. Then,

several spectra were calculated using all combinations of $D\sigma$ and $D\tau$ values ranging from -1.0 to +1.0 eV. The $D\sigma$ parameter shows itself marginally sensitive compared to $D\tau$. Variations of $D\sigma$ between 0.5 and 0.7 eV barely affect the Cr $2p$ XPS. Conversely, variations of only 0.01 eV of $D\tau$ open a wide range of features, as we will discuss afterwards. Hence, for both 5 and 23 ML samples, we set the value of $D\sigma$ to +0.600 eV.

For fixed values of Dq and $D\sigma$, **Figure 4** shows that the $D\tau$ parameter controls the relative energies between the valence orbitals [28,31–34], which determine different fine structure for the XPS spectra. For $D\tau$ positive (not shown) or lower than -0.34 eV (left of region I), the Cr $2p_{3/2}$ envelope appears mostly as a single asymmetrical peak. As $D\tau$ value decreases from 0 to -0.34 eV, the relative intensity of the multiplet peaks changes, leading to a progressive decrease in the intensity of the multiplet peak at lower binding energy and the appearance of a shoulder at the left of the main peak (high-energy part). Hence, for optimal Dq (0.208 eV) and $D\sigma$ (0.600 eV), two ranges of $D\tau$ values (**Figure 4**) are particularly interesting for our study: region I where $-0.330 < D\tau < -0.290$ eV for spectra simulation of first epilayers, and region II where $-0.280 < D\tau < -0.260$ eV for thicker samples.

Indeed, the splitting and the relative stabilities of d-orbitals are closely related to the values of CFM parameters. Thus, the lower the value of $D\tau$ (**Figure 4**), the lower the energy of the e orbitals and the higher energy of the a_1 orbital. In region I, the $a_1(t_{2g})$ orbital is destabilized in relation to the $e(t_{2g})$ orbital, whereas in region II these orbitals are almost at the same energy level. Their exact degeneracy is at $D\tau = -0.27$ eV. The splitting between the orbital triplets ($t_{2g} \rightarrow a_1 + e$) is a consequence of lowering the Oh symmetry of the CrO_6 octahedral center to C_{3v}. As a result, the orbital destabilization

seen in the XPS spectrum for the first Cr_2O_3 epilayers is an evidence of the trigonal distortions of the oxygen octahedron around the Cr^{3+} cation in this stage of growth.
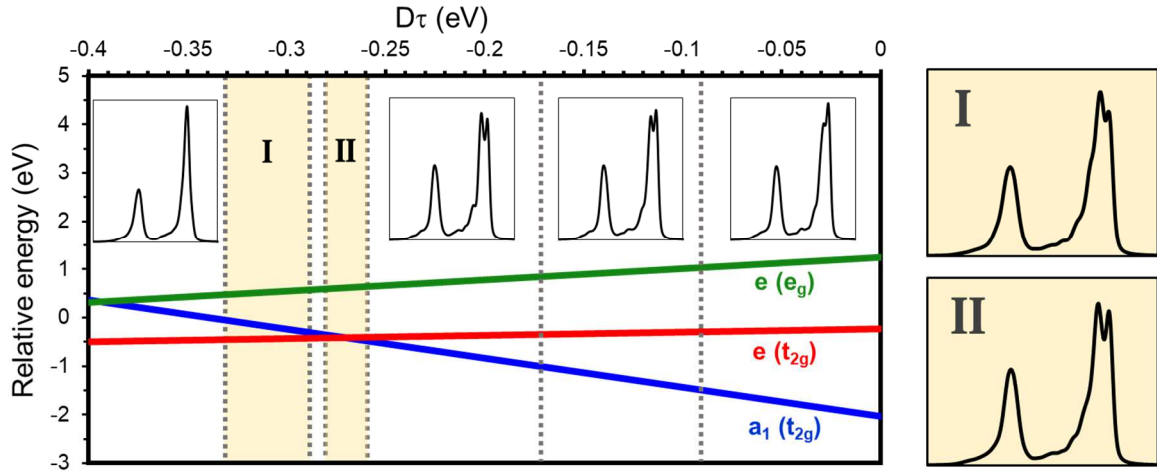

Figure 4. Evolution of the Cr^{3+} calculated spectral shape (inset at top) with the $D\tau$ parameter when $D\sigma = 0.60$ eV and $10Dq = 2.08$ eV. Highlighted in the right the calculated spectral shape for region I and II, which correspond to the optimal values of $D\tau$ to simulate the spectra of first epilayers and thicker samples, respectively. The relative energies of the valence orbitals ($a_1(t_{2g})$ blue, $e(t_{2g})$ red and $e(e_g)$ green line) are determined by the CF parameters through the relationship: $a_1(t_{2g}) = -4Dq - 2D\sigma - 6D\tau$, $e(t_{2g}) = -4Dq + D\sigma + 2/3\, D\tau$, and $e(e_g) = +6Dq + 7/3\, D\tau$.

3.4 Geometry considerations

To analyze more precisely the relationships between the XPS spectra and possible structural changes, RHEED patterns of the O-MBE samples have been recorded as a function of the coverage (**Figure 5**). The in-plane lattice mismatch for α-Cr_2O_3 (a = 0.492 nm) growing on α-Al_2O_3 (a = 0.476 nm) being +3.36 %, a compressive strain is expected at the early stages of the growth with a progressive relaxation of the in-plane

lattice parameter to a value close to that of bulk α-Cr$_2$O$_3$. The RHEED patterns exhibit sharp streaks for 5 M□ and 23 M□, proving the high crystalline quality of the monolayers and the existence of a bidimensional growth mode. No spots or extra streaks are observed, indicating the lack of secondary phases. According to the spacing between the (11) and ($\bar{1}\bar{1}$) streaks extracted from the RHEED images (**Figure 5**), we clearly confirm that the first epilayers are under significant lateral compression of 3.36 % for 5 M□ (*i.e.* same streak position than the substrate). Meanwhile, the cell parameter of the 23 M□ film has already relaxed by about 1.91 %, imposing a residual in-plane strain of 1.45 %.
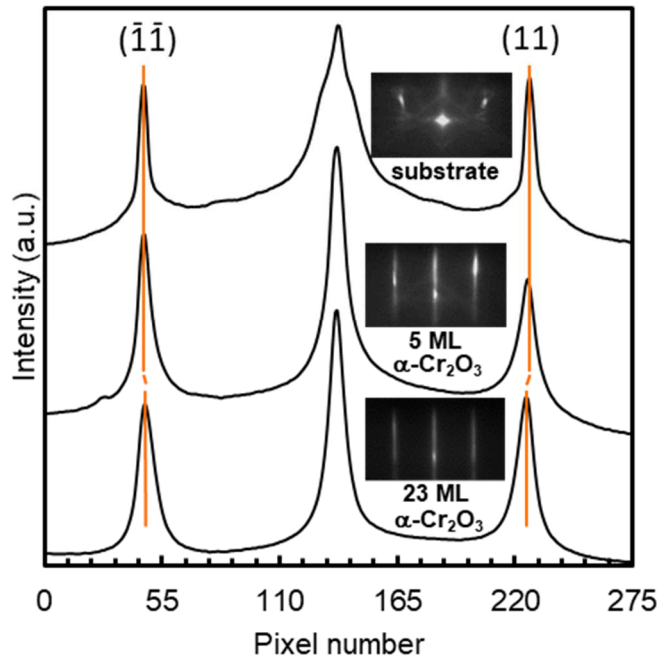

Figure 5. RHEED patterns and extracted profile lines as a function of Cr$_2$O$_3$ film thickness: at the top, the α-Al$_2$O$_3$(0001) substrate, at the middle, the 5 M□ and at the bottom, 23 M□ α-Cr$_2$O$_3$(0001) film. The electron beam is aligned along the [1$\bar{1}$00] crystallographic orientation.

15

For the 5 ML Cr_2O_3 spectrum, the precise set of CF parameters that best fitted the experimental data is $Dq = 0.208$ eV, $D\sigma = 0.600$ eV and $D\tau = -0.295$ eV $\pm$ 0.005 (**Figure 6a**), while the 23 ML Cr_2O_3 spectrum is well fitted with $Dq = 0.208$ eV, $D\sigma = 0.600$ eV and $D\tau = -0.280$ eV $\pm$ 0.005 (**Figure 6b**). The orbital diagram determined by those parameters for the 23 ML sample (**Figure 6b**, top left) shows a small splitting between the a_1 and e orbitals of about 70 meV. This energy splitting is consistent with the literature [31], where the trigonal CF parameter for this T-state is calculated as ~2 meV in a fully relaxed Cr_2O_3 crystal. On the other hand, the orbital diagram of the 5 ML sample (**Figure 6a**, top left) shows a larger splitting of the t_{2g} orbital (~170 meV), where a_1 orbital rises in energy while the e orbital falls.

In the C_{3v} model [35], the components of the t_{2g} set are z^2 for a_1 and a linear combination of the other d components for e (see Supporting Information). By compressing the xy plane, the top three as well as the bottom three ligands move closer together [36,37] (**Figure 6a**, top right). This distortion limits the space of the z^2 component, oriented along the C_3 axis, and a_1 is destabilized. Hence, the increasing energy of a_1 orbital in relation to e orbital for the first epilayers is a consequence of the compression in the xy plane imposed by the lattice mismatch between α-Al_2O_3 and α-Cr_2O_3. These results are then in good agreement with the evolution observed in the RHEED patterns shown in **Figure 5** and also with the analysis of the RHEED patterns and high-resolution TEM micrographs reported in literature [11,38].

Similar evolution of the XPS spectra has also been reported for α-Cr_2O_3 epitaxial films growing on Pt(111) [13,39]. Yet, divergent interpretations were given for the XPS spectra, mainly provided by electron diffraction patterns (LEED or RHEED) of the initial stages of growth. Zhang *et al.* [39] suggested that a metastable cubic spinel

Cr$_3$O$_4$(111) layers composes the first stages of deposition with simultaneous presence of Cr^{2+} and Cr^{3+}. Meanwhile, in a more recent work, Chambers and Droubay [13] interpreted the broad Cr 2p spectrum as being due to the formation of a metastable γ-Cr$_2$O$_3$ layer with Cr^{3+} ions distributed among tetrahedral and octahedral sites. We provide a different explanation in light of the results obtained for α-Cr$_2$O$_3$ grown on α-Al$_2$O$_3$. The evolution of the XPS spectra for α-Cr$_2$O$_3$ epitaxial films on Pt(111) is more probably related to in-plane strain generated by the compressive misfit of 2 %, which gently decreases with growth.
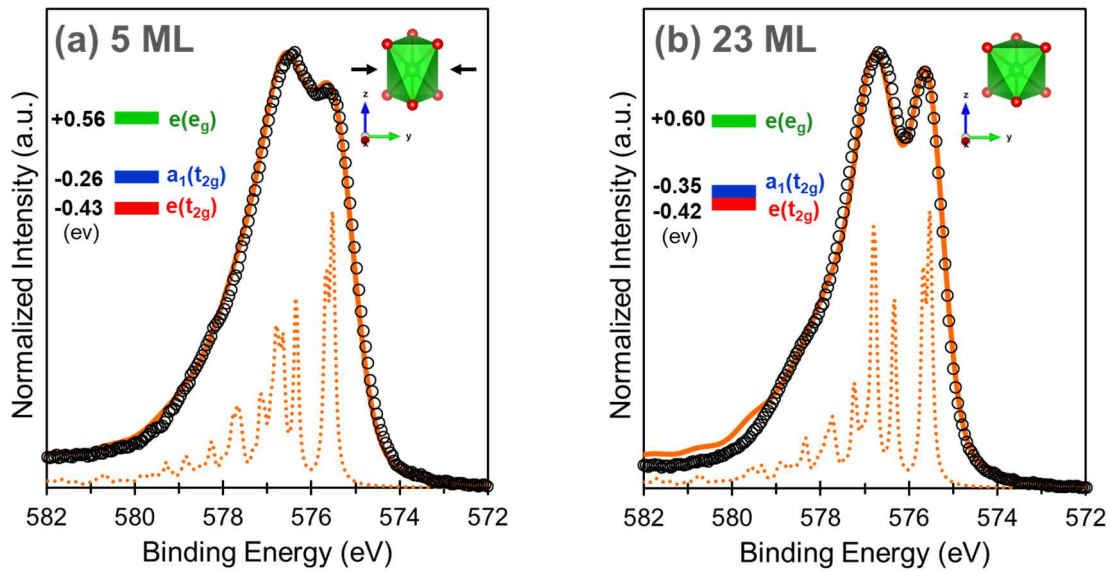
Figure 6. Calculated Cr 2p XPS spectra (orange line) in comparison with the experimental spectra (black circles) for 5 M□ (a) and 23 M□ (b) of α-Cr$_2$O$_3$(0001) thin films grown on α-Al$_2$O$_3$(0001) substrates. Below each experimental spectrum, the theoretical spectrum (dotted line) with stick diagrams (FWHM = 0.1 eV) are shown. At the top left, the 3d orbital diagram is plotted for 10Dq = 2.08 eV, $D\sigma$ = 0.60 eV, $D\tau$ = -0.295 ± 0.005 eV (a) and $D\tau$ = -0.280 ± 0.005

eV (b). At the top right, a schematic representation of the octahedral distortion is depicted. Color coding: Cr (green) and O (red).

3.5 Crystal field parameters for oxidation layers

The CF parameters for the Cr_2O_3 spectra acquired during the oxidation of Ni30Cr alloy were derived out of the results obtained for the O-MBE films. The Dq and $D\sigma$ values were kept to 0.208 eV and 0.600 eV respectively, while the $D\tau$ parameter was adjusted to give the best fit possible to the experimental spectra. Similar to the epitaxial films, $D\tau$ progressively increase with the oxide growth, taking a value of -0.329 ± 0.001 eV at $t = 4$ min or 4.4 nm (**Figure 7a**), -0.325 ± 0.001 eV at $t = 9$ min or 8.1 nm (**Figure 7b**), and -0.26 ± 0.01 eV at $t = 25$ min or 15.5 nm (**Figure 7c**).

The fitting of the Cr $2p_{3/2}$ envelope is not perfect for the polycrystalline samples at very early oxidation stage (**Figure 7**a). Indeed, polycrystalline samples exhibit several local structures, which may naturally broad the peaks in comparison to the calculated spectrum. Moreover, at the very beginning of the oxide layer growth, chemisorbed oxygen may be attached to the metallic surface and the Cr cations may be not complete oxidized. This is suggested by the O $1s$ XPS spectra shown in **Figure S4** in SI. Significant shifts towards lower energies of the core-level O $1s$ are observed as the oxidation proceeds: relative to the bulk ($t = 25$ min), the O $1s$ shifts by 1.0 eV and 0.5 eV in the $t = 1$ and 4 min films, respectively. In addition, the O $1s$ line at $t = 4$ min sample is very large, indicating two different degrees of oxidation for the oxygen species. Similar trends were found during the initial oxidation reaction on the Ni-Cr alloys surface years ago [40,41].

Even if the model cannot fully describe the spectrum at the very beginning of the alloy-to-oxide transformation, geometry statements can be done for the evolution of Cr

18

XPS spectra from 4 to 25 minutes of oxidation. One striking feature is the increase of the parameter $D\tau$ with oxidation time – or sample thickness – from -0.329 ± 0.001 up to -0.26 ± 0.01. This corresponds to the decrease of the splitting of e and a_1 orbitals to full degeneracy (**Figure 4**). CrO$_6$ octahedra are therefore significantly distorted with respect to their C$_{3v}$ site symmetry at the beginning of the oxidation, and then gently relax as the oxidation proceeds. As a result, strains of α-Cr$_2$O$_3$ layer develop during Ni30Cr oxidation in a similar manner as for epitaxial layers, keeping in mind that the strain is in-plane during the oxidation growth and that the α-Cr$_2$O$_3$ layer align its c-axis preferentially perpendicular to the surface.
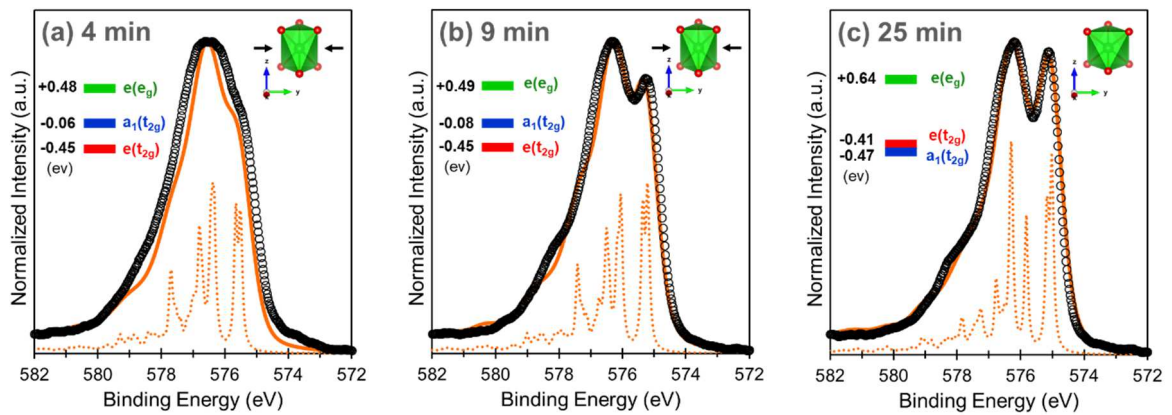
Figure 7. Calculated Cr 2p XPS spectra (orange line) in comparison with the experimental spectra (black circles) for 4 min (a), 9 min (b) and 25 min (c) of exposure of the alloy to the oxygen flow. Below each experimental spectrum, the theoretical spectrum (dotted line) with stick diagrams (FWHM = 0.1 eV) are shown. At the top left, the $3d$ orbital diagram (a$_1$(t$_{2g}$) blue, e(t$_{2g}$) red and e(e$_g$) green line) is plotted for $D\tau = -0.329 \pm 0.001$ eV (a), $D\tau = -0.325 \pm 0.001$ eV (b) and $D\tau = -0.26 \pm 0.01$ eV (c).

Some piece of information available in literature corroborate our findings. Actually, the existence of residual stress and its relaxation with thickness is known for a long time [42]. Residual stresses for α-Cr_2O_3 layer growing on Ni30Cr are usually compressive, in the order of few GPa [4,43]. Additionally, recent experiments [6,44] point out that the growth of α-Cr_2O_3 layer operates along the c-axis during the oxidation of Ni30Cr alloys and also in pure chromium. Interestingly, similar evolution of the Cr $2p$ XPS spectrum with oxidation time has been also reported for both systems [6,45], featuring a very strong splitting of the Cr $2p_{3/2}$ peak for thick layer.

The growth stresses and relaxation mechanisms are intimately related to the detailed mechanism of oxide growth. As shown in Section 3.4, for α-Cr_2O_3 grown epitaxially on Al_2O_3 (0001), the strain energy accumulates rapidly with film thickness due to the lattice mismatch of +3.36 %. This system undergoes strain relief by nucleating misfit dislocations and relaxes completely up to few nanometers [11]. However, for polycrystalline Cr_2O_3 grown by Ni30Cr oxidation, the residual stress is a complex summation of growth stresses and thermal stresses. The system relaxes via creep and the critical thickness depends on the growth kinetics and the microstructure of chromia scales [42]. In our study, a relaxed chromium oxide layers upon Ni30Cr oxidation were found at tens of nanometers.

Whatever the microstructure (MBE layers [11], oxidation layers [45] or polycrystalline powder [46]), the "relaxed" α-Cr_2O_3 layer provides a well-defined splitting of the Cr $2p_{3/2}$ XPS envelope. It coincides to a fully degeneracy of e and a_1 orbitals according to our estimation by CFM, with $D\tau$ closes to -0.27 eV. As a result, well-defined splitting of Cr $2p_{3/2}$ XPS envelope can be considered as a fingerprint of well relaxed CrO_6 octahedra in α-Cr_2O_3.

4. CONCLUSIONS

We have investigated the photoemission spectra acquired during the growth of α-Cr_2O_3 layers by Ni30Cr alloy oxidation and by chromium and oxygen co-evaporation in the O-MBE setup. In both cases, the Cr $2p_{3/2}$ XPS envelope changes as the layer thickens, featuring gradually a discernable splitting of the band and a shoulder in the high-energy part. Herein, a comprehensive link between these spectral shape evolutions and the local structure of the α-Cr_2O_3 layers has been established by means of Crystal Field Multiplet calculations.

In the CFM approach, three crystal field parameters Dq, $D\sigma$ and $D\tau$ are required to describe the relative energies of d-orbitals – $a_1(t_{2g})$, $e(t_{2g})$ and $e(e_g)$ – of Cr^{3+} in its C_{3v} site symmetry. After careful evaluation of those parameter using the XPS spectra of high quality epitaxial α-Cr_2O_3 thin films grown by O-MBE, we have shown that only one parameter ($D\tau$) controls the relative energies of the d-orbitals. These relative energies are related to trigonal distortions of the local Cr^{3+} local environment and drives the fine structure of Cr $2p_{3/2}$ XPS. Hence, the broad band of Cr $2p_{3/2}$ XPS observed for the first O-MBE epilayers originates from a sizeable in-plane strain of α-Cr_2O_3 – imposed by the compressive misfit with α-Al_2O_3 substrate – which translates in large trigonal distortions of CrO_6 octahedra. Conversely, the visible splitting of Cr $2p_{3/2}$ XPS arising for thick layer relies on relaxed CrO_6 octahedra, encountered in bulk α-Cr_2O_3.

Interestingly, using CFM calculations we are able to revisit the microstructure of the α-Cr_2O_3 polycrystalline layer, which grows during the oxidation Ni30Cr. We have

evidenced that (*i*) an in-plane strain does exist in α-Cr$_2$O$_3$ layer up to thickness of 8.1 nm; (*ii*) α-Cr$_2$O$_3$ crystallite shows a preferential orientation along the c-axis in the hexagonal setting; and (*iii*) there is a strain relaxation with thickening.

More broadly, we believe that the shape and features of the Cr 2$p_{3/2}$ XPS measured in α-Cr$_2$O$_3$ can be used as structural tool when combined with CFM calculations. Such an approach reveals to be very effective since it calls only for XPS measurements and requires calculations with low computational cost.

5. REFERENCES

[1] S. Fyfitch, Corrosion and Stress Corrosion Cracking of Ni-Base Alloys, in: Compr. Nucl. Mater., Elsevier, 2012: pp. 69–92.

[2] W. Kuang, M. Song, G.S. Was, Insights into the stress corrosion cracking of solution annealed alloy 690 in simulated pressurized water reactor primary water under dynamic straining, Acta Mater. 151 (2018) 321–333.

[3] A.H. Heuer, H. Kahn, F. Ernst, G.M. Michal, D.B. Hovis, R.J. Rayne, F.J. Martin, P.M. Natishan, Enhanced corrosion resistance of interstitially hardened stainless steel: Implications of a critical passive layer thickness for breakdown, Acta Mater. 60 (2012) 716–725.

[4] M. Kemdehoundja, J.F. Dinhut, J.L. Grosseau-Poussard, M. Jeannin, High temperature oxidation of Ni70Cr30 alloy: Determination of oxidation kinetics and stress evolution in chromia layers by Raman spectroscopy, Mater. Sci. Eng. A. 435–436 (2006) 666–671.

[5] E. Schmucker, C. Petitjean, L. Martinelli, P.-J. Panteix, S. Ben Lagha, M. Vilasi, Oxidation of Ni-Cr alloy at intermediate oxygen pressures. I. Diffusion mechanisms through the oxide layer, Corros. Sci. 111 (2016) 474–485.

[6] L. Bataillou, L. Martinelli, C. Desgranges, S. Bosonnet, K. Ginestar, F. Miserque, Y. Wouters, L. Latu-Romain, A. Pugliara, A. Proietti, D. Monceau, Growth Kinetics and Characterization of Chromia Scales Formed on Ni–30Cr Alloy in Impure Argon at 700 °C, Oxid. Met. (2020).

[7] W.H. Blades, P. Reinke, From Alloy to Oxide: Capturing the Early Stages of Oxidation on Ni–Cr(100) Alloys, ACS Appl. Mater. Interfaces. 10 (2018) 43219–43229.

[8] L. Luo, L. Zou, D.K. Schreiber, M.J. Olszta, D.R. Baer, S.M. Bruemmer, G. Zhou, C.-M. Wang, In situ atomic scale visualization of surface kinetics driven dynamics of oxide growth on a Ni–Cr surface, Chem. Commun. 52 (2016) 3300–3303.

[9] L. Marchetti, F. Miserque, S. Perrin, M. Pijolat, XPS study of Ni-base alloys oxide films formed in primary conditions of pressurized water reactor, Surf. Interface Anal. 47 (2015) 632–642.

[10] V. Maurice, G. Despert, S. Zanna, P. Josso, M.-P. Bacos, P. Marcus, XPS study of the initial stages of oxidation of α2-Ti3Al and γ-TiAl intermetallic alloys, Acta Mater. 55 (2007) 3315–3325.

[11] S.A. Chambers, Y. Liang, Y. Gao, Noncommutative Band Offset at α-Cr$_2$O$_3$/α-Fe$_2$O$_3$(0001) Heterojunctions, Phys. Rev. B. 61 (2000) 13223–13229.

[12] C. Palacio, H.J. Mathieu, D. Landolt, AES, XPS and EELS study of the initial oxidation of polycrystalline chromium, Surf. Sci. 182 (1987) 41–55.

[13] S.A. Chambers, T. Droubay, Role of oxide ionicity in electronic screening at oxide/metal interfaces, Phys. Rev. B. 64 (2001).

[14] M.C. Biesinger, B.P. Payne, A.P. Grosvenor, L.W.M. Lau, A.R. Gerson, R.St.C. Smart, Resolving surface chemical states in XPS analysis of first row transition metals, oxides and hydroxides: Cr, Mn, Fe, Co and Ni, Appl. Surf. Sci. 257 (2011) 2717–2730.

[15] R.P. Gupta, S.K. Sen, Calculation of multiplet structure of core p -vacancy levels. II, Phys. Rev. B. 12 (1975) 15–19.

[16] M.C. Biesinger, C. Brown, J.R. Mycroft, R.D. Davidson, N.S. McIntyre, X-ray photoelectron spectroscopy studies of chromium compounds, Surf. Interface Anal. 36 (2004) 1550–1563.

[17] R.E. Newnham, Y.M. Haan, Refinement of the α-Al_2O_3, Ti_2O_3, V_2O_3 and Cr_2O_3 structures, Z. Für Krist. (1962) 235–237.

[18] R.G. Burns, Mineralogical Applications of Crystal Field Theory, Cambridge University Press, 1993.

[19] M.O.J.Y. Hunault, Y. Harada, J. Miyawaki, J. Wang, A. Meijerink, F.M.F. de Groot, M.M. van Schooneveld, Direct Observation of Cr^{3+} $3d$ States in Ruby: Toward Experimental Mechanistic Evidence of Metal Chemistry, J. Phys. Chem. A. 122 (2018) 4399–4413.

[20] Y. Tanabe, M. Muto, E. Hanamura, Theory of nonlinear optical susceptibilities of antiferromagnetic Cr_2O_3, Solis State Commun. 102 (1997) 643–646.

[21] J.-B. Moussy, From epitaxial growth of ferrite thin films to spin-polarized tunnelling, J. Phys. Appl. Phys. 46 (2013) 143001.

[22] M.W. Haverkort, G. Sangiovanni, P. Hansmann, A. Toschi, Y. Lu, S. Macke, Bands, resonances, edge singularities and excitons in core level spectroscopy investigated within the dynamical mean-field theory, Europhys. Lett. 108 (2014) 57004.

[23] M.W. Haverkort, M. Zwierzycki, O.K. Andersen, Multiplet ligand-field theory using Wannier orbitals, Phys. Rev. B. 85 (2012).

[24] Y. Lu, M. Höppner, O. Gunnarsson, M. W. Haverkort, Efficient real frequency solver for dynamical mean field theory, Phys. Rev. B. 90 (2014).

[25] M. Retegan, Crispy: version 0.7.3, 2019.

[26] F. De Groot, A. Kotani, Core level spectroscopy of solids. CRC Press, Boca Raton, (2008).

[27] R.D. Cowan, The theory of atomic structure and spectra, University of California Press: Berkeley, CA, 1981.

[28] V. Vercamer, M.O.J.Y. Hunault, G. Lelong, M.W. Haverkort, G. Calas, Y. Arai, H. Hijiya, L. Paulatto, C. Brouder, M.-A. Arrio, A. Juhin, Calculation of optical and K pre-edge absorption spectra for ferrous iron of distorted sites in oxide crystals, Phys. Rev. B. 94 (2016) 245115–1–245115–15.

[29] E. Ünveren, E. Kemnitz, S. Hutton, A. Lippitz, W.E.S. Unger, Analysis of highly resolved x-ray photoelectron Cr $2p$ spectra obtained with a Cr_2O_3 powder sample prepared with adhesive tape, Surf. Interface Anal. 36 (2004) 92–95.

[30] M. Aronniemi, J. Sainio, J. Lahtinen, Chemical state quantification of iron and chromium oxides using XPS: the effect of the background subtraction method, Surf. Sci. 578 (2005) 108–123.

[31] M.G. Brik, N.M. Avram, C.N. Avram, Crystal field analysis of energy level structure of the Cr_2O_3 antiferromagnet, Solid State Commun. 132 (2004) 831–835.

[32] E. Konig, S. Kremer, Ligand field: energy diagrams, Plenum Press, New York, 1977.

[33] P.H. Butler, Point Group Symmetry Applications: Methods and Tables, Springer US, Boston, MA, 1981.

[34] A. Juhin, C. Brouder, M.-A. Arrio, D. Cabaret, P. Sainctavit, E. Balan, A. Bordage, A.P. Seitsonen, G. Calas, S.G. Eeckhout, P. Glatzel, X-ray linear dichroism in cubic compounds: The case of Cr^{3+} in $MgAl_2O_4$, Phys. Rev. B. 78 (2008) 1–19.

[35] S.K. Kang, H. Tang, T.A. Albright, Structures for d^0 ML_6 and ML_5 complexes, J. Am. Chem. Soc. 115 (1993) 1971–1981.

[36] S. Mu, K.D. Belashchenko, Influence of strain and chemical substitution on the magnetic anisotropy of antiferromagnetic Cr_2O_3: An *ab-initio* study, Phys. Rev. Mater. 3 (2019).

[37] T.C. Kaspar, S.E. Chamberlin, M.E. Bowden, R. Colby, V. Shutthanandan, S. Manandhar, Y. Wang, P.V. Sushko, S.A. Chambers, Impact of lattice mismatch and stoichiometry on the structure and bandgap of $(Fe,Cr)_2O_3$ epitaxial thin films, J. Phys. Condens. Matter. 26 (2014) 135005.

[38] S.A. Chambers, Epitaxial growth and properties of thin film oxides, Surf. Sci. Rep. (2000) 105–180.

[39] L. Zhang, M. Kuhn, U. Diebold, Growth, structure and thermal properties of chromium oxide films on Pt(111), Surf. Sci. 375 (1997) 1–12.

[40] S.-P. Jeng, P.H. Holloway, C.D. Batich, Surface passivation of Ni/Cr alloy at room temperature, Surf. Sci. 227 (1990) 278–290.

[41] J.-C. Dupin, D. Gonbeau, P. Vinatier, A. Levasseur, Systematic XPS studies of metal oxides, hydroxides and peroxides, Phys. Chem. Chem. Phys. 2 (2000) 1319–1324.

[42] S.J. Bull, Modeling of Residual Stress in Oxide Scales, Oxid. Met. 49 (1998) 17.

[43] J. Mougin, T. Le Bihan, G. Lucazeau, High-pressure study of Cr_2O_3 obtained by high-temperature oxidation by X-ray diffraction and Raman spectroscopy, J. Phys. Chem. Solids. 62 (2001) 553–563.

[44] L. Latu-Romain, Y. Parsa, S. Mathieu, M. Vilasi, M. Ollivier, A. Galerie, Y. Wouters, Duplex n- and p-Type Chromia Grown on Pure Chromium: A Photoelectrochemical and Microscopic Study, Oxid. Met. 86 (2016) 497–509.

[45] J.-T. Li, V. Maurice, J. Swiatowska-Mrowiecka, A. Seyeux, S. Zanna, L. Klein, S.-G. Sun, P. Marcus, XPS, time-of-flight-SIMS and polarization modulation IRRAS study of Cr2O3 thin film materials as anode for lithium ion battery, Electrochimica Acta. 54 (2009) 3700–3707.

[46] B.P. Payne, M.C. Biesinger, N.S. McIntyre, X-ray photoelectron spectroscopy studies of reactions on chromium metal and chromium oxide surfaces, J. Electron Spectrosc. Relat. Phenom. 184 (2011) 29–37.

Cr 2$p_{3/2}$ XPS

e(e_g)

a$_1$(t$_{2g}$)

e(t$_{2g}$)

e(e_g)

a$_1$(t$_{2g}$)

e(t$_{2g}$)

strain relaxation